Quantifying mass flows at Mt. Cleveland, Alaska between 2001 and 2020 using satellite photogrammetry

Chunli Dai [a,*], Ian M. Howat [b], Jeffrey T. Freymueller [c], Zhong Lu [d], Saurabh Vijay [e], Anna K. Liljedahl [f], Melissa K. Ward Jones [g], Helena Bergstedt [g], Einat Lev [h]

[a] *Department of Civil and Environmental Engineering, Louisiana State University, Baton Rouge, LA, USA*
[b] *Byrd Polar and Climate Research Center, The Ohio State University, Columbus, OH, USA*
[c] *Department of Earth and Environmental Sciences, Michigan State University, East Lansing, MI, USA*
[d] *Roy M. Huffington Department of Earth Sciences, Southern Methodist University, Dallas, TX, USA*
[e] *Department of Civil Engineering, Indian Institute of Technology Roorkee, Roorkee, Uttarakhand, India*
[f] *Woodwell Climate Research Center, Falmouth, MA, USA*
[g] *Water and Environmental Research Center, University of Alaska Fairbanks, Fairbanks, AK, USA*
[h] *Lamont-Doherty Earth Observatory, Columbia University, Palisades, NY, USA*

ARTICLE INFO

ABSTRACT

Measuring eruption volume provides constraints on the magma supply rate and plumbing systems and therefore is a critical component for monitoring volcanoes. We use ArcticDEM—a large collection of time-dependent digital elevation models (DEMs) derived from satellite stereo-photogrammetry — to construct a first-of-its-kind measurement of the volumes of recent mass flows at Mount Cleveland, Alaska. We quantify the volume of the products of the 2001 eruption (the largest in the past half-century) as $(54.8 \pm 0.5) \times 10^6 \, \text{m}^3$ covering a total area of 5.09 km^2. The total volume of material loss at the summit crater is $(0.67 \pm 0.02) \times 10^6 \, \text{m}^3$, which is likely caused by later explosions and collapses of the shallow magma chamber. The total eruptive volume between 2017 and 2020 is $(0.086 \pm 0.002) \times 10^6 \, \text{m}^3$. Elevation changes associated with lahars are variable. On the upper northern slopes of the volcano, the lahar channels were almost exclusively erosive, suggesting that lahars originating at the summit eroded and entrained loose materials high on the cone. In general, lahar deposits were thickest near their toes, with some reaching ~20 m thickness.

1. Introduction

Mount Cleveland volcano, located in the central Aleutian Islands of Alaska, is one of the most active volcanoes in North America. Aleutian Island Arc volcanoes are formed from the subduction of the Pacific plate beneath the North American plate. The rate of plate convergence is about 7 cm/year near Mount Cleveland (Power et al., 2021). Mount Cleveland is considered to be an open-vent system where volcanic products erupt without producing significant deformation outside the summit crater (Lu and Dzurisin, 2014; Power et al., 2021). It has erupted 37 times in the past 250 years (Smith, 2005), among which 24 eruptions occurred within the past 37 years (since 1984). Since 2001, four major eruptions (with a volcanic explosivity index (VEI) >3) occurred in 2001, 2006, 2013–2014, and 2020, according to the Alaska Volcano Observatory (https://avo.alaska.edu/volcanoes/volcact.php?volcname=Cle

veland, last accessed May 23, 2022). The 2001 eruption produced substantial lava flows (Smith, 2005), while the later ones were primarily explosive and produced vigorous eruption plumes and some lahars. During a single eruption, Mount Cleveland usually produces several different types of eruptive products including gas emissions, ash plumes, lahars, pyroclastic debris flows, and effusive lava flows (Smith, 2005). Although this volcano is located in a remote area, volcanic ash plumes from Cleveland eruptions pose a high risk to heavily traveled air routes, with the potential to cause severe damage to aircraft (e.g., Dean and Dehn, 2015).

Integrated remote sensing, geophysical, and geological data can improve our knowledge of past eruption behaviors and magmatic processes, which may facilitate eruption forecasts and warnings. The 2001 eruption at Mount Cleveland was the largest in the past half-century (Power et al., 2021). Dean et al. (2004) investigated the extent of lava
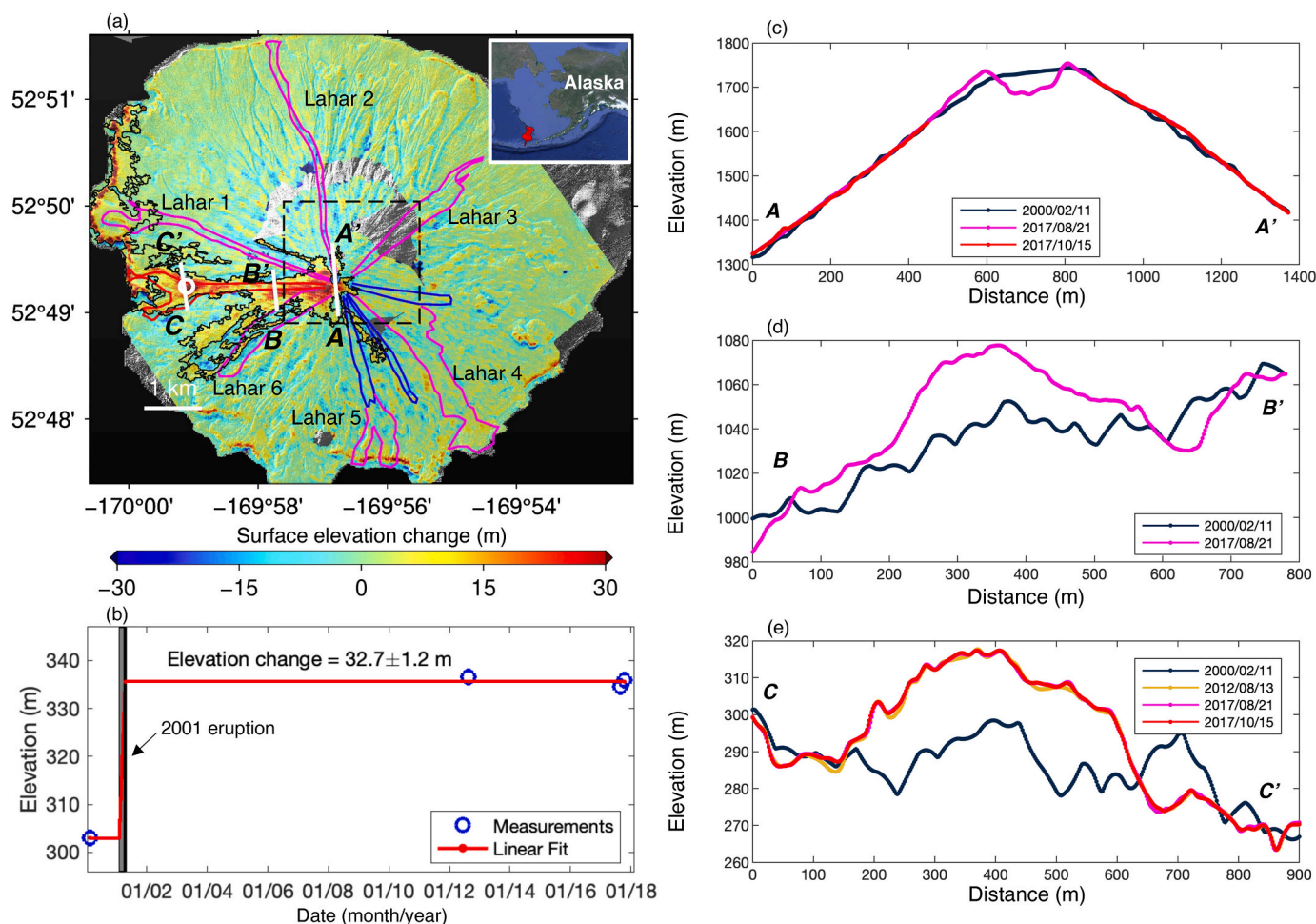
Fig. 1. Surface elevation changes of Cleveland Volcano between 2000 and 2012. (a) Surface elevation change estimated from multiple Digital Elevation Models (DEMs) (Table S1). The background is the hillshade of 2-m resolution DEM generated from DigitalGlobe/Maxar WorldView-2 images acquired on August 23, 2020. The black lines outline the mass flow field retrieved from the surface elevation change map. The lahar/lava flows (blue lines), lahar flows (magenta lines), and lava flow (red line) boundaries of the 2001 eruption from field observations and satellite images (Smith, 2005) are plotted. The black box denotes the study area in Fig. 3. The inset shows the location (red pin) of Mount Cleveland on Google Earth map. (b) The elevation time series at the white circle in (a). The blue circles are elevation measurements from SRTM DEM and ArcticDEM. Red line is the linear fit (Eq. (1)) to satellite measurements (blue circles). The black vertical bar denotes the time span of the 2001 eruption. (c-e) Surface elevation profiles across the lava flow field AA', BB', and CC'. The location of the profiles is denoted in Fig. 1 (a). The pre-eruptive DEM (black) is the SRTM DEM acquired in February 2000. The post-eruptive DEMs are ArcticDEM data (denoted in colour orange, magenta, and red). Note that the DEM in August 2012 is not available along AA' (c) and BB' (d) profiles due to data gaps near the summit (see also Fig. S1). (For interpretation of the references to colour in this figure legend, the reader is referred to the web version of this article.)

flows from this eruption using satellite thermal data (AVHRR, 1 km resolution) and the extent of deposits using Landsat 7 (30 m) and satellite radar data (Radarsat, 30 m resolution), as well as the motion of volcanic clouds at different stages using satellite images from multiple missions (GOES, AVHRR, and MODIS). Smith (2005) quantified the lava effusion rates of the 2001 eruption using thermal infrared data and mapped the mass flow extents using Landsat 7 images and field observations, yielding a volume estimate of 9.1×10^6 m³. Wang et al. (2015) studied dome formation associated with eruptive activity at Mount Cleveland in 2011–2012 using TerraSAR-X radar imagery, giving a volume estimate of 0.9×10^6 m³ for part of the 2011 eruption. Werner et al. (2017) estimated the total volume extruded from 2011 to 2015 eruptions as $(1.9–5.8) \times 10^6$ m³ using satellite thermal infrared data (MODIS). The combination of gas emission and melt inclusion data for the 2016 eruption at Mount Cleveland volcano suggested a continued presence of shallow magma in the upper conduit between 0.5 and 3 km depth (Werner et al., 2020). The recent availability of on-site seismic data (since 2014) also suggested a shallow magma body fed by a deeper conduit system (Power et al., 2021).

Despite these previous studies, little is known about the distribution

of past eruptive flows at Cleveland Volcano, which are crucial for understanding associated eruptive volumes and processes. Different satellite missions have been used for studying active volcanism worldwide, e.g., the TanDEM-X radar satellite mission can overcome obscurity from clouds or nighttime measurements and provide lava flow maps at 15 m resolution (e.g., Kubanek et al., 2015, 2017), and Pleiades-1 optical satellites can provide time series of volcanic topography at 1 m resolution (Bagnardi et al., 2016; Moussallam et al., 2021). However, these data have limited accessibility. This paper quantifies the surface elevation changes corresponding to 2001, 2017–2019, and 2020 eruptions of Mt. Cleveland, Alaska using multiple remote sensing datasets. We analyze changes in surface elevation by integrating Digital Elevation Models (DEMs) from the Shuttle Radar Topography Mission (SRTM) (Farr et al., 2007) and ArcticDEM (Porter et al., 2018). The 30 m resolution SRTM DEMs acquired in February 2000 provide the earliest acquisition of the topography for this study. ArcticDEM, generated from commercial satellite imagery, provides 2-m resolution DEMs for the last decade. Here, the unprecedented spatial and temporal coverage of ArcticDEM enables the first detailed quantification of the spatial distribution of the mass flows at Mt. Cleveland two decades after its major

2001 eruption.

2. Data and methods

2.1. WorldView DEMs

We obtain high-resolution (2 m) DEMs created from stereoscopic satellite imagery acquired by the WorldView constellation of satellites. Eleven of these DEMs, created from imagery acquired between 2010 and 2018, were created and distributed as part of the ArcticDEM project (Porter et al., 2018). ArcticDEM data are generated using the SETSM software (Noh and Howat, 2015, 2017) from stereo pairs of images obtained either along the same orbital pass, or from different orbital passes where the differences in view angles are sufficient (Noh and Howat, 2019). Considering that the quality of stereo-photogrammetric DEMs is affected by clouds, shadow, surface water, or saturation artifacts in satellite imagery (Dai and Howat, 2018), we manually scrutinized the quality of each available DEM. Since Mount Cleveland has seasonal snow cover each winter (Smith, 2005), we selected DEMs between August and October to minimize snow coverage on the volcanic cone. A comparison of winter and summer DEMs suggests that seasonal snowpack on the upper slopes is on the order of several meters thick. Manual selection based on data quality and snow cover leads to three good quality DEMs (Table S1) from the eleven available DEMs.

In order to quantify the mass flows of the latest June 1, 2020 eruption, we requested a satellite acquisition shortly after the eruption (in July 2020) via the USGS Commercial Remote Sensing Space Policy (CRSSP) Imagery Derived Requirements (CIDR) tool (https://cidr.cr.usgs.gov/). We received three WorldView-2 images on August 23 and two WorldView-1 images on August 24 through the NextView license (Neigh et al., 2013). Three DEMs (Table S2) were then created from stereoscopic imagery collected in 2020 using the same software as that used by the ArcticDEM project (SETSM, Noh and Howat, 2015). Detailed mapping of the recent 2020 eruption demonstrates the recent morphological changes of the summit crater.

2.2. DEM coregistration and time series analysis

DEM coregistration is required to reduce systematic planar and rotational offsets between each pair of DEMs (Fig. S1) (Dai and Howat, 2017). We adopt the algorithm developed by Noh and Howat (2014), which automatically selects control points based on similarities in DEM slope, aspect, and height undulations. Control points are those stable pixels where no relative movement is detected (e.g., Fig. S2 in Dai and Howat, 2017). The coregistration is well defined when the number of control points is sufficient (>0.3% of all pixels) and evenly distributed, as well as height differences over control points following a Gaussian distribution (Noh and Howat, 2014). To mitigate the impact of areas of topographic change on DEM coregistration, we also manually crop out the lava flow areas. The DEM with the best coverage is chosen as the reference DEM, e.g., the SRTM DEM in 2000, or the ArcticDEM on August 23, 2020. For eruptions between 2000 and 2012, the mean height difference over automatically detected control points after the coregistration is around 0.03 m, and the standard deviation of height differences over control points is about 5 m. For eruptions between 2017 and 2020, the mean and standard deviation over control points are around 0.004 m and 0.8 m, respectively. The worse performance for the 2000–2012 eruptions is caused by the inclusion of SRTM DEM (Dai and Howat, 2017), which has lower vertical accuracy. Here, the 30-m resolution SRTM DEM is resampled to 2-m posting for differencing with the 2-m resolution DEMs.

Next, the surface elevation time series at each pixel is analyzed based on the time series analysis method of Dai and Howat (2017). A simple linear model with least-squares adjustment is used to estimate the surface elevation change caused by volcanic eruptions, and quantify the corresponding uncertainties (e.g., Fig. 1(b)). The linear model is defined
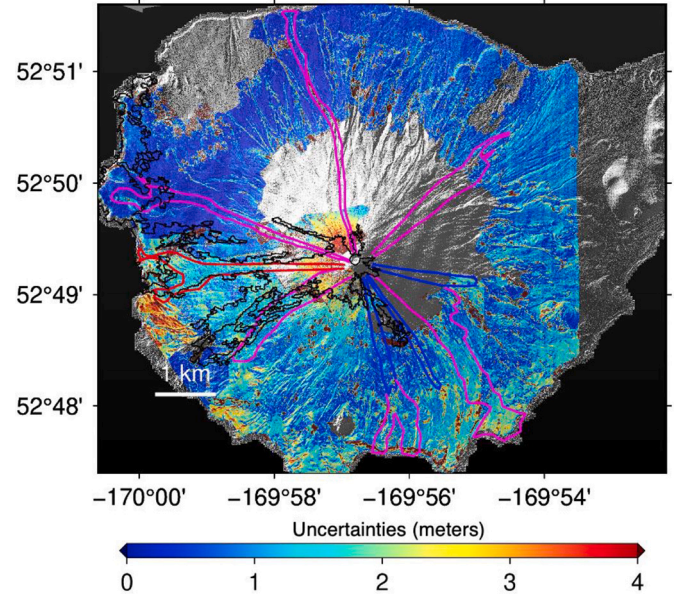

Fig. 2. Uncertainty of the estimated elevation change between 2000 and 2012. The background is the hillshade of 2-m resolution DEM generated from WorldView-2 images acquired on August 23, 2020. The black lines outline the mass flow field retrieved from the surface elevation change map (Fig. 1(a)). The blue, magenta, and red lines denote the lahar/lava flows, lahar flows, and lava flow boundaries of the 2001 eruption from field observations and satellite images (Smith, 2005). The average uncertainty is about 1.5 m, and the median uncertainty is about 0.9 m. (For interpretation of the references to colour in this figure legend, the reader is referred to the web version of this article.)

by a constant value and a change of elevation using the Heaviside step function. We have:

$$y = a + b \times H(t - t_e) \tag{1}$$

where y is the surface elevation (in meters) measured at acquisition time (t in years), and t_e is the epoch of the eruption from the Global Volcanism Program or other published sources, in years. a is the constant representing surface elevation before the eruption in unit of meters, b is the estimated elevation change, in meters. $H(t - t_e)$ is the Heaviside step function as shown in Dai and Howat (2017).

The uncertainties are estimated through the error propagation of the estimated variance component, $\hat{\sigma}_0^2$, which can be calculated by the following equation:

$$\hat{\sigma}_0^2 = \tilde{e}^T P \tilde{e}/(n - m)$$

where n is the total number of DEM acquisitions. m is the number of unknown parameters (e.g., the elevation change, b, and the surface elevation before the eruption, a), which is 2 here. $\tilde{e}$ is the estimated error vector (n by 1) of all measurements, where each element of this vector is the difference between a measurement and the linear fit to all measurements (Fig. 1b). P is the weight matrix (n by n), which is a unit matrix by assuming equal weight for all measurements. The square root of the estimated variance component represents the uncertainty of elevation measurements at each pixel. The uncertainties of estimated parameters (i.e., the elevation change) can then be estimated through error propagation. It is worth pointing out that there was a typographical error in eq. 4 of Dai and Howat (2017), where the denominator should be (n-m) instead of (n-1) for the estimated variance component, $\hat{\sigma}_0^2$.
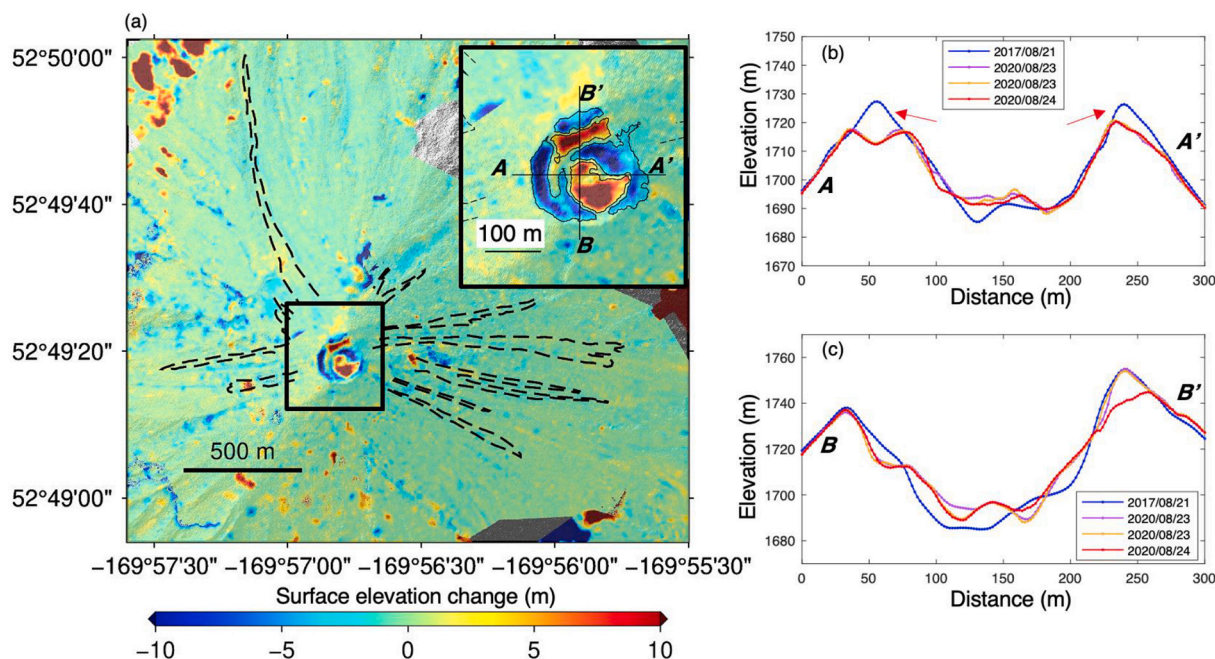
Fig. 3. Surface elevation changes between 2017 and 2020. (a) The surface elevation change map. The black dash lines are digitized mass-flow deposits of the 2020 eruption outlined by Chris Waythomas at the Alaska Volcano Observatory (https://www.avo.alaska.edu/images/image.php?id=159631). The inset shows the enlargement of the summit area, and the black thin lines denote the boundaries of the deposits and material loss. (b)-(c) Surface elevation profiles along two profiles across the summit area.

2.3. Post processing of the surface elevation change map

After retrieving the 2D surface elevation change (e.g., Fig. 1) from the DEM time series analysis, additional filtering and post processing steps are carried out to remove outliers and fill small voids. First, we filter out pixels that have uncertainties larger than 10 m (around five times the average uncertainty) (e.g., Fig. 2). Afterward, small areas of voids are interpolated with a maximum distance of 15 pixels (30 m) from the edges of valid data. The post-processed surface elevation change data is then used to estimate the volumes and areas of mass flows (Dai and Howat, 2017).

3. Results

3.1. 2001 eruption

Due to the limited temporal resolution of DEM measurements (Table S1), we can only solve for the total topographic change between February 2000 and August 2012 (Fig. 1). During this period, the largest eruption series occurred in 2001 (VEI 3). Another relatively large eruption in 2006 was characterized by high explosive plumes, and gas and ash emissions, but did not produce noticeable volcanic deposits at the volcano (Neal et al., 2009). There were eight smaller eruptions (VEI 2), all of them primarily explosive. Details about the eruption from February 2 to April 15, 2001 can be found at the Global Volcanism Program, Smithsonian Institution (https://volcano.si.edu/;McGimsey et al., 2004). There is no evidence to suggest that the smaller eruptions, or even the 2006 VEI 3 eruption, produced substantial flow deposits, so our estimated surface elevation changes primarily represent the flows from the 2001 eruption, except at the summit area where subsequent changes to the summit crater dominate the signal.

Based on the surface elevation change map from multiple DEMs (Fig. 1(a)), the mass flow area is determined by selecting pixels with elevation changes >2 m. The threshold of 2 m is chosen corresponding to the average uncertainty of estimated elevation changes (Fig. 3). Small clusters of data with total areas <20,000 m^2 are removed, and small

holes with total areas <4000 m^2 are restored. We then identify the mass flow field (Fig. 1) as the largest cluster of positive surface elevation changes in the vicinity of the mapped lava field by Smith (2005). Based on the algorithms for estimating the eruption volume and its uncertainty (Welch, 1967; Bagnardi et al., 2016; Dai and Howat, 2017), the total volume is then estimated to be $(54.8 \pm 0.5) \times 10^6$ m^3, and the total area is 5.09 km^2. For the calculation of the volume uncertainty, the covariance between neighboring pixels is estimated using the average periodogram of surface elevation changes in four stable regions (no mass flows) marked in Fig. S2 (Dai et al., 2020). In areas with no standard deviations (due to lack of repeated measurements), the mean standard deviation (1.5 m) of surface elevation changes is used to fill the void. Our estimated total volume from the DEM time series is about 4 times larger than the estimate of Smith (2005), a volume of 9.1×10^6 m^3, which was made from a rough estimate of the flow extent using satellite data and an assumption of a 10 m average thickness for the lava flow. The difference mainly results from the larger area (5.09 km^2) of flow extent quantified in this study using DEMs. The flow deposit area was estimated to be only 0.85 km^2 by Smith (2005), but he also noted that his estimate was limited by the lack of field observations at higher elevations (>300 m). Based on DEM differencing, we find that there were large deposits at higher elevations as well. Our deposit field extent generally agrees with the Smith (2005) deposit outlines of the 2001 eruption at the lower elevations, where his outlines were based on field mapping.

The summit area shows both positive and negative elevation changes, including the development of a prominent summit crater. Material gain near the summit is focused on the southern and western rim of the crater, and including the uppermost parts of the main flow deposits. Material loss at the summit reflects the development of a prominent summit crater. The total 2000–2012 material loss at the summit area is estimated from the area showing >2 m surface elevation decrease. The total area of elevation loss is 0.021 km^2, and the total volume of material loss is about $(0.67 \pm 0.02) \times 10^6$ m^3. The summit area was likely modified many times by the eruptions between 2001 and 2012, so it is not possible to identify deformation or destruction caused
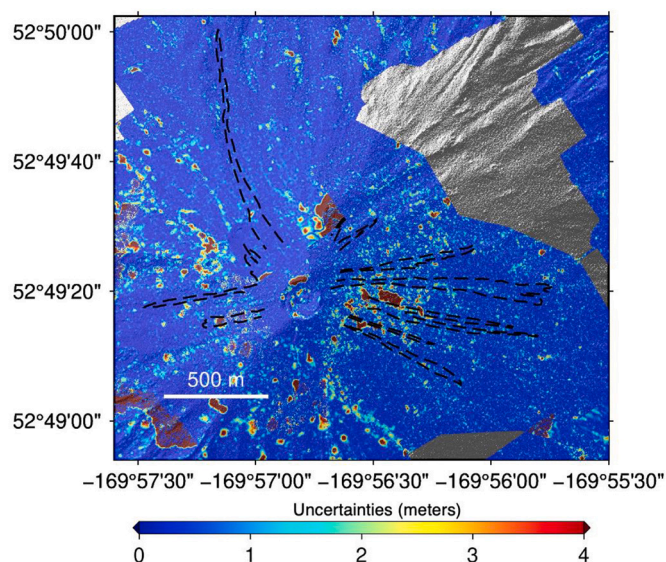
Fig. 4. Uncertainty of the estimated elevation change between 2017 and 2020. The background is the hillshade of 2-m resolution DEM generated from Maxar WorldView-2 images acquired on August 23, 2020. The black dash lines are digitized mass-flow deposits outlined by Chris Waythomas at the Alaska Volcano Observatory (https://www.avo.alaska.edu/images/image.php?id=159631, last accessed May 26, 2022). The average uncertainty is about 2.2 m, and the median uncertainty is about 0.2 m.

by a single eruption. However, field photos, satellite images, and photos taken by the International Space Station give some information about the evolution of the summit crater as discussed in Section 4.

3.2. Surface elevation changes between 2017 and 2020

In recent years, satellite images have observed repeated lava dome growth and destruction (by explosions) within Mount Cleveland's summit crater (e.g., Wang et al., 2015; Werner et al., 2017, 2020). On June 1, 2020, an explosion was detected by regional infrasound sensors. The Alaska Volcano Observatory reported that this eruption blew out the January 2019 dome and some material from the summit crater (http://www.avo.alaska.edu), and volcanic debris flows (of unknown thickness) extended 2.8 km down the northern and eastern flanks of the volcano. With a timely request of the satellite tasking to this area, we generated three post-eruptive DEMs in August 2020 (Table S2), which provided a valuable data source for mapping recent eruptions.

Since the latest pre-eruptive DEMs were in 2017 (Table S2), we can only solve for the total surface elevation changes between 2017 and 2020. There were three eruptions during this period: the February 3, 2017 to January 20, 2019 eruption, the November 7 to November 15, 2019 eruption, and the June 1, 2020 eruption (https://avo.alaska.edu/volcanoes/volcact.php?volcname=Cleveland). The measured topographic changes (Fig. 3) represent the total changes from these three eruptions between August 21, 2017 and June 1, 2020.

As shown in Fig. 3(b), the most prominent feature is that part of the rim of the summit crater was removed during these eruptions, but there are also areas within the crater that show elevation gain. The boundary of the largest area of elevation increase (Fig. 3(a)) is consistent with the location of the lava dome that formed in January 2019 (https://avo.alaska.edu/images/image.php?id=150661), and likely represents the remnants of that dome. With a threshold of 2 m, the total volume change within the area of surface elevation increase within the crater is about $(0.086 \pm 0.002) \times 10^6$ m^3, with a total area of 0.01 km^2. The average standard deviation of the estimated surface elevation change from DEM time series is about 2.2 m (Fig. 4). The uncertainty of the total volume is estimated using the same method as described before (Bagnardi et al.,

2016; Dai and Howat, 2017). Height increase in this area likely represents the remains of a dome or domes extruded within the crater, which was then partially destroyed by later explosions. With a threshold of -2 m, the total volume of material loss along the rim of the crater is about $(0.12 \pm 0.01) \times 10^6$ m^3, with a total area of 0.02 km^2. Given that these elevation decreases correspond to the location of the crater rim as of 2017, it is likely that these materials were blasted away by the series of explosions, which in places widened the crater, near A (Fig. 3b).

Outside the crater, we did not observe clear elevation changes that could be related to volcanic activity. The total area within the mapped (by the Alaska Volcano Observatory) debris flows of the 2020 eruption is 0.22 km^2 and the net volume is $(-0.04 \pm 0.01) \times 10^6$ m^3, yielding a mean thickness of about -0.2 ± 0.05 m, which is not significant considering the uncertainties of the elevation change (e.g., around 2.2 m of mean uncertainty). Fig. 3a shows some small areas of apparent height increase or decrease, but these do not correspond to the mass flow deposits mapped for the 2020 eruption, nor do their shapes clearly point to a volcanic origin. The lack of clear flow deposits in the DEM difference map, in contrast to the large deposits observed for the 2001 eruption, suggests that any proximal deposits were too thin to be resolved given the current accuracy of stereo-photogrammetric DEMs.

4. Discussion

Smith (2005) reported a rounded profile of the summit (without ice) in 2002, and a partial collapse of the southern portion of the crater that occurred between summer 2002 and July 2004. For example, International Space Station photo ISS004 Roll: E Frame: 13801 (Fig. S3a) shows a rounded and snow-topped summit in May 2002, while other images taken later in the same summer show a rounded and snow-free summit (e.g., Fig. S3b). In contrast, photos (Fig. S3c) and field observations from July 2004 show a clear cut-out at the summit that was not present in 2002 (Smith, 2005). Hence, our estimated material loss between 2000 and 2012 is probably dominated by a collapse at the summit following the 2001 eruption. However, our estimate may also reflect later modification of the summit crater by later explosions. Very few photos of the Cleveland summit exist during that time period, but photos from pilot Chad Hults in August 2008 (Fig. S3d) show a larger and differently shaped summit crater than was observed in 2004 by Smith.

The bowl-shaped depression at the summit (Fig. 1c, Fig. S3d) is likely caused by both the later explosions (definition of a crater) and the collapse of the shallow magma chamber after the effusion of lava, which is the definition of a caldera. Specifically, field photos of the partial collapse during an inactive period (Smith, 2005) indicate that the second mechanism explains part of the material loss at the summit. Depressurization of the magma chamber or degassing would cause the surface elevation decrease. In addition, there is evidence from later seismic data (Power et al., 2013, 2021) and gas emissions analysis (Werner et al., 2020) suggesting the persistent existence of a shallow magma in the magma conduit system, and the top of the magma column within hundreds of meters depth. It is likely that both mechanisms have contributed to the total observed mass loss at the summit crater (i.e., $(0.67 \pm 0.02) \times 10^6$ m^3).

Outside the summit crater, the 2001 flow deposits include lava flows, lahar flows, and volcaniclastic debris flows. The depositional sequence described by Smith (2005) showed that the 2001 eruption produced a thick layer of volcaniclastic debris on the bottom and then a layer of lava flows on top. The lack of data on the fraction and density of each type of material makes it difficult to convert the bulk volume to the dense-rock equivalent (DRE) of magma (Dai and Howat, 2017; Dai et al., 2020). Assuming the nonvesiculated magma density of 2600 kg/m^3 (Werner et al., 2020) and potential average flow densities of 1300–2600 kg/m^3, spanning the range of lahars, debris flows and 'a'a lava flows (Belousov and Belousova, 2018; Thouret et al., 2020), gives a plausible range of $(27–55) \times 10^6$ m^3 DRE of erupted magma.

One of the error sources in elevation changes is due to snow coverage

Table 1
The volume and area of deposits within each lahar. Note: The main deposits and the material loss are not included in the calculation for peripheral areas.

	For all peripheral areas	Lahar 1	Lahar 2	Lahar 3	Lahar 4	Lahar 5	Lahar 6
Volume	$(-1.8 \pm 1) \times 10^6$ m^3	$(0.8 \pm 0.3) \times 10^6$ m^3	$(-0.7 \pm 0.1) \times 10^6$ m^3	$(-0.1 \pm 0.1) \times 10^6$ m^3	$(3.0 \pm 0.2) \times 10^6$ m^3	$(0.9 \pm 0.1) \times 10^6$ m^3	$(2.3 \pm 0.3) \times 10^6$ m^3
Area	54 km^2	0.64 km^2	0.46 km^2	0.79 km^2	1.7 km^2	0.6 km^2	0.78 km^2
Average thickness	-0.03 ± 0.02 m	1.3 ± 0.5 m	-1.6 ± 0.2 m	-0.1 ± 0.1 m	1.7 ± 0.1 m	1.5 ± 0.2 m	2.9 ± 0.4 m
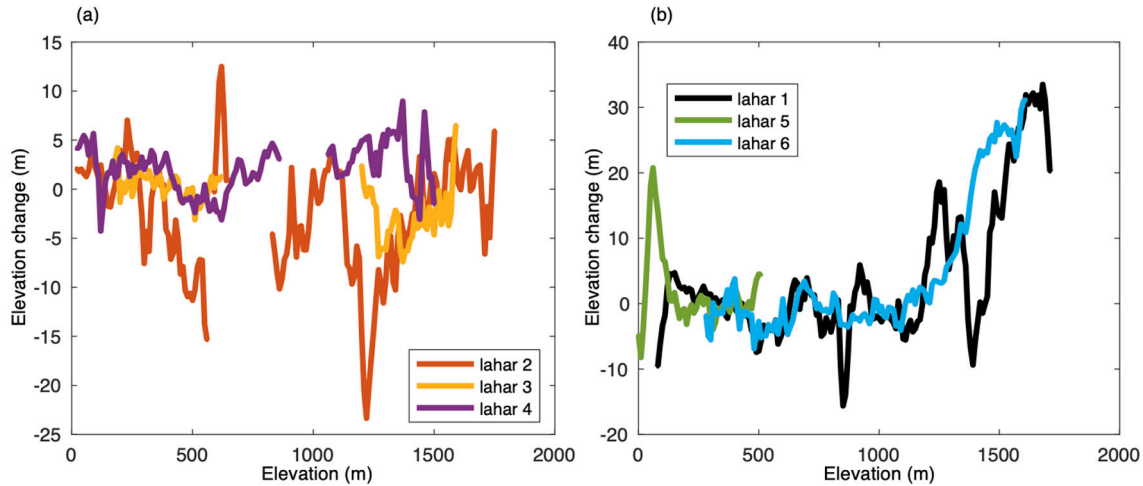
Fig. 5. Elevation change profiles along each lahar. The *y*-axis represents the median elevation changes within a bin (interval) of absolute elevations. The spatial boundary of each lahar is shown in Fig. 1(a).

at the acquisition time (February 2000) of the SRTM DEM. Nevertheless, considering the penetration of the C-band radar signal of SRTM into snow up to 10 m (Gardelle et al., 2012), the effect of snow coverage is expected to be negligible based on our estimate for seasonal snow accumulation of a few to several meters based on the later winter optical DEMs. The average elevation change of all pixels outside of the main mass flow fields is around -0.03 ± 0.02 m (Table 1). This near-zero average over peripheral areas is expected since the coregistration of DEMs is designed to minimize the elevation differences at the control points located on the stable rocky terrain. This quantity is a good measure for evaluating the overall coregistration performance.

Six lahars (Fig. 1a) were identified by Smith (2005) based on mapping and interpretation of field photos and satellite images. The elevation profiles along the six lahars (Fig. 5) show that erosion is dominant during the study period on the northern side of the volcano, especially on the steep slopes. Lahars were formed primarily by volcanic ash or other debris, which melted snow near the summit and resulted in meltwater and mud flowing down the steep slope. Some of these flows likely eroded the pre-eruptive topography and entrained additional loose materials on the upper slopes, eventually depositing material on the lower flanks (or into the ocean). Lahars 2 and 3 on the north show predominantly near-zero or negative elevation changes (Fig. 5a), especially at higher elevations, and the net volume changes within these two mapped lahars are negative (Table 1). Lahar 2 appears to have reached the ocean, so material likely was deposited mainly offshore. The lahars on the western and southern slopes (1, 5, 6) show elevation gain on the higher slopes (with limited areas of apparent erosion in the case of lahar 1), and smaller elevation changes at lower elevations (Fig. 5b). Lahar 5 on the southern slope shows a large elevation increase at its toe, up to 20 m thick (Fig. 5b). The thick deposits along lahars 1 and 6 may include part of the main mass flow field (black line in Fig. 1a).

5. Conclusion

Here we characterize the topographic changes caused by historical eruptions between 2001 and 2020 using 2 m resolution DEM time series generated from commercial satellite imagery. ArcticDEM offers a unique data source for recovering high resolution mass flow distribution maps and volume estimates 20 years after the 2001 eruption. In addition, following timely satellite tasking, elevation changes caused by the June 1, 2020 eruption were mapped two months after the event.

Topographic changes at Mount Cleveland over 2000–2020 are mainly associated with the large flow deposits caused by the 2001 eruption, and with the subsequent modification of the summit by collapses and explosions. We quantify the volume of the lava and debris flows of the largest eruption (2001) as $(54.8 \pm 0.5) \times 10^6$ m^3 (likely $(27–55) \times 10^6$ m^3 DRE of magma), and the flow deposits covered a total area of 5.09 km^2. Flow deposits on the upper slopes of the volcano are much thicker than reported by Smith (2005), who could only access the lower portion of the flows, hence yielded a much less volume estimate $(9.1 \times 10^6$ m^3). The total volume of material loss (2001−2012) at the summit crater is $(0.67 \pm 0.02) \times 10^6$ m^3, which is likely caused by explosions and collapses of the shallow magma chamber starting sometime between 2002 and July 2004 and continuing through several explosive eruptions. The total eruptive volume between 2017 and 2020 is only $(0.086 \pm 0.002) \times 10^6$ m^3. A comparison of the 2017 and 2020 images quantifies the changes at the summit, which included removal of parts of the crater rim, and the remnant of an extrusive dome within the summit crater.

Elevation changes associated with the 2001 lahars are variable. On the upper northern slopes of the volcano, the lahar channels were almost exclusively erosive, suggesting that lahars originating at the summit eroded and entrained loose materials high on the cone. These lahars produced deposits on the lower slopes, aside from one lahar that reached the ocean and likely deposited material offshore. Other lahars were

predominantly depositional, with little evidence of erosion on the steep, upper slopes.

For active volcanoes, more frequent satellite revisits of the target area would be essential for differentiating individual eruptions. Our methodology of synthesizing multiple DEMs through time series analysis is a useful approach for overcoming the common issue of data gaps in DEMs from optical images. Our results reaffirm and highlight the potential for DEM time series to be an important tool in monitoring and studying volcanic activity.

CRediT authorship contribution statement

Chunli Dai: Conceptualization, Methodology, Software, Writing – original draft. **Ian M. Howat:** Supervision, Writing – review & editing. **Jeffrey T. Freymueller:** Validation, Formal analysis, Writing – review & editing. **Zhong Lu:** Validation. **Saurabh Vijay:** Validation. **Anna K. Liljedahl:** Resources, Writing – review & editing. **Melissa K. Ward Jones**: Writing – review & editing. **Helena Bergstedt**: Writing – review & editing. **Einat Lev**: Writing – review & editing.

Declaration of Competing Interest

The authors declare that they have no known competing financial interests or personal relationships that could have appeared to influence the work reported in this paper.

Acknowledgments

Appendix A. Supplementary data

Supplementary data to this article can be found online at https://doi.org/10.1016/j.jvolgeores.2022.107614.

References

Bagnardi, M., González, P.J., Hooper, A., 2016. High-resolution digital elevation model from tri-stereo Pleiades-1 satellite imagery for lava flow volume estimates at Fogo Volcano. Geophys. Res. Lett. 43 (12), 6267–6275.

Belousov, A., Belousova, M., 2018. Dynamics and viscosity of 'a'a and pahoehoe lava flows of the 2012–2013 eruption of Tolbachik volcano, Kamchatka (Russia). Bull. Volcanol. 80 (6) https://doi.org/10.1007/s00445-017-1180-2.

Dai, C., Howat, I.M., 2017. Measuring lava flows with ArcticDEM: Application to the 2012–2013 eruption of Tolbachik, Kamchatka. Geophys. Res. Lett. 44 (24), 12–133.

Dai, C., Howat, I.M., 2018. Detection of saturation in high-resolution Pushbroom satellite imagery. IEEE J. Select. Top. Appl. Earth Observ. Remote Sens. 11 (5), 1684–1693.

Dai, C., Howat, I.M., Freymueller, J.T., Vijay, S., Jia, Y., 2020. Characterization of the 2008 phreatomagmatic eruption of Okmok from ArcticDEM and InSAR: Deposition, erosion, and deformation. J. Geophys. Res. Solid Earth 125 (6) (p.e2019JB018977).

Dean, K.G., Dehn, J., 2015. Monitoring Volcanoes in the North Pacific: Observations from Space. Springer Science & Business Media.

Dean, K.G., Dehn, J., Papp, K.R., Smith, S., Izbekov, P., Peterson, R., Kearney, C., Steffke, A., 2004. Integrated satellite observations of the 2001 eruption of Mt. Cleveland, Alaska. J. Volcanol. Geotherm. Res. 135 (1–2), 51–73.

Farr, T.G., Rosen, P.A., Caro, E., Crippen, R., Duren, R., Hensley, S., Kobrick, M., Paller, M., Rodriguez, E., Roth, L., Seal, D., 2007. The shuttle radar topography mission. Rev. Geophys. 45 (2).

Gardelle, J., Berthier, E., Arnaud, Y., 2012. Impact of resolution and radar penetration on glacier elevation changes computed from DEM differencing. J. Glaciol. 58 (208), 419–422.

Kubanek, J., Richardson, J.A., Charbonnier, S.J., Connor, L.J., 2015. Lava flow mapping and volume calculations for the 2012–2013 Tolbachik, Kamchatka, fissure eruption using bistatic TanDEM-X InSAR. Bull. Volcanol. 77 (12), 1–13.

Kubanek, J., Westerhaus, M., Heck, B., 2017. TanDEM-X time series analysis reveals lava flow volume and effusion rates of the 2012–2013 Tolbachik, Kamchatka fissure eruption. J. Geophys. Res. Solid Earth 122 (10), 7754–7774.

Lu, Z., Dzurisin, D., 2014. InSAR Imaging of Aleutian Volcanoes. In InSAR Imaging of Aleutian Volcanoes. Springer, Berlin, Heidelberg, pp. 87–345.

McGimsey, R.G., Neal, C.A., Girina, O., 2004. 2001 Volcanic Activity in Alaska and Kamchatka: Summary of Events and Response of the Alaska Volcano Observatory. U. S. Geological Survey Scientific Investigations Report 2004–1453, pp. 16–26 available at URL: https://pubs.usgs.gov/of/2004/1453/of2004-1453.pdf (last accessed May 26, 2022).

Moussallam, Y., Barnie, T., Amigo, Á., Kelfoun, K., Flores, F., Franco, L., Cardona, C., Cordova, L., Toloza, V., 2021. Monitoring and forecasting hazards from a slow growing lava dome using aerial imagery, tri-stereo Pleiades-1A/B imagery and PDC numerical simulation. Earth Planet. Sci. Lett. 564, 116906.

Neal, C.A., McGimsey, R.G., Dixon, J.P., Manevich, A., Rybin, A., 2009. 2006 Volcanic activity in Alaska, Kamchatka, and the Kurile Islands: Summary of events and response of the Alaska Volcano Observatory. U.S. Geological Survey Scientific Investigations Report 2008–5214, pp. 57–60 available at URL: https://pubs.usgs.gov/sir/2008/5214/pdf/sir20085214.pdf (last accessed May 26, 2022).

Neigh, C.S., Masek, J.G., Nickeson, J.E., 2013. High-resolution satellite data open for government research. EOS Trans. Am. Geophys. Union 94 (13), 121–123.

Noh, M.J., Howat, I.M., 2014. Automated coregistration of repeat digital elevation models for surface elevation change measurement using geometric constraints. IEEE Trans. Geosci. Remote Sens. 52 (4), 2247–2260.

Noh, M.J., Howat, I.M., 2015. Automated stereo-photogrammetric DEM generation at high latitudes: Surface Extraction with TIN-based Search-space Minimization (SETSM) validation and demonstration over glaciated regions. GIScience Remote Sens. 52 (2), 198–217.

Noh, M.J., Howat, I.M., 2017. The surface extraction from TIN based search-space minimization (SETSM) algorithm. ISPRS J. Photogramm. Remote Sens. 129, 55–76.

Noh, M.J., Howat, I.M., 2019. Applications of High-Resolution, Cross-Track, Pushbroom Satellite Images with the SETSM Algorithm. IEEE J. Select. Top. Appl. Earth Observ. Remote Sens. 12 (10), 3885–3899.

Porter, C., Morin, P., Howat, I., Noh, M.J., Bates, B., Peterman, K., Keesey, S., Schlenk, M., Gardiner, J., Tomko, K., Willis, M., 2018. Arctic DEM, Harvard DataVerse, vol. 1. Polar Geospatial Center, University of Minnesota, St. Paul, Minnesota, USA.

Power, J.A., Stihler, S.D., Chouet, B.A., Haney, M.M., Ketner, D.M., 2013. Seismic observations of Redoubt Volcano, Alaska—1989–2010 and a conceptual model of the Redoubt magmatic system. J. Volcanol. Geotherm. Res. 259, 31–44.

Power, J.A., Roman, D.C., Lyons, J.J., Haney, M.M., Rasmussen, D.J., Plank, T., Nicolaysen, K.P., Izbekov, P., Werner, C., Kaufman, A.M., 2021. Volcanic seismicity beneath Chuginadak Island, Alaska (Cleveland and Tana volcanoes): Implications for magma dynamics and eruption forecasting. J. Volcanol. Geotherm. Res. 412, 107182.

Smith, S.J., 2005. Chronologic Multisensor Assessment for Mount Cleveland, Alaska from 2000 to 2004 Focusing on the 2001 Eruption (Doctoral dissertation).

Thouret, J.-C., Antoine, S., Magill, C., Ollier, C., 2020. Lahars and debris flows: Characteristics and impacts. Earth Sci. Rev. 201 (103003) https://doi.org/10.1016/j.earscirev.2019.103003.

Wang, T., Poland, M.P., Lu, Z., 2015. Dome growth at Mount Cleveland, Aleutian Arc, quantified by time series TerraSAR-X imagery. Geophys. Res. Lett. 42 (24), 10–614.

Welch, P., 1967. The use of fast Fourier transform for the estimation of power spectra: a method based on time averaging over short, modified periodograms. IEEE Trans. Audio Electroacoust. 15 (2), 70–73.

Werner, C., Kern, C., Coppola, D., Lyons, J.J., Kelly, P.J., Wallace, K.L., Schneider, D.J., Wessels, R.L., 2017. Magmatic degassing, lava dome extrusion, and explosions from Mount Cleveland volcano, Alaska, 2011–2015: Insight into the continuous nature of

volcanic activity over multi-year timescales. J. Volcanol. Geotherm. Res. 337, 98–110.

Werner, C., Rasmussen, D.J., Plank, T., Kelly, P.J., Kern, C., Lopez, T., Gliss, J., Power, J. A., Roman, D.C., Izbekov, P., Lyons, J., 2020. Linking subsurface to surface using gas emission and melt inclusion data at Mount Cleveland volcano, Alaska. Geochem. Geophys. Geosyst. 21 (7) (p.e2019GC008882).

Wessel, P., Smith, W.H., 1991. Free software helps map and display data. EOS Trans. Am. Geophys. Union 72 (41), 441–446.